

# The statistics of $\Lambda$ CDM Halo Concentrations

Angelo F. Neto<sup>1,2\*</sup>, Liang Gao<sup>2</sup>, Philip Bett<sup>2</sup>, Shaun Cole<sup>2</sup>, Julio F. Navarro<sup>2,3†</sup>, Carlos S. Frenk<sup>2</sup>, Simon D.M. White<sup>4</sup>, Volker Springel<sup>4</sup>, Adrian Jenkins<sup>2</sup>

<sup>1</sup>*Instituto de Física, Universidade Federal do Rio Grande do Sul, Porto Alegre RS, Brazil*

<sup>2</sup>*Institute of Computational Cosmology, Department of Physics, University of Durham, Science Laboratories, South Road, Durham DH1 3LE, UK*

<sup>3</sup>*Department of Physics and Astronomy, University of Victoria, PO Box 3055 STN CSC, Victoria, BC, V8W 3P6 Canada*

<sup>4</sup>*Max-Planck Institute for Astrophysics, Karl-Schwarzschild Str. 1, D-85748, Garching, Germany*

1 February 2008

## ABSTRACT

We use the *Millennium Simulation (MS)* to study the statistics of  $\Lambda$ CDM halo concentrations at  $z = 0$ . Our results confirm that the average halo concentration declines monotonically with mass; a power-law fits well the concentration-mass relation for over 3 decades in mass, up to the most massive objects to form in a  $\Lambda$ CDM universe ( $\sim 10^{15} h^{-1} M_{\odot}$ ). This is in clear disagreement with the predictions of the model proposed by Bullock et al. for these rare objects, and agrees better with the original predictions of Navarro, Frenk, & White. The large volume surveyed, together with the unprecedented numerical resolution of the *MS*, allow us to estimate with confidence the distribution of concentrations and, consequently, the abundance of systems with unusual properties. About one in a hundred cluster haloes ( $M_{200} \gtrsim 3 \times 10^{14} h^{-1} M_{\odot}$ ) have concentrations exceeding  $c_{200} = 7.5$ , a result that may be used to interpret the likelihood of unusually strong massive gravitational lenses, such as Abell 1689, in the  $\Lambda$ CDM cosmogony. A similar fraction (1 in 100) of galaxy-sized haloes ( $M_{200} \sim 10^{12} h^{-1} M_{\odot}$ ) have  $c_{200} < 4.5$ , an important constraint on models that attempt to reconcile the rotation curves of low surface-brightness galaxies by appealing to haloes of unexpectedly low concentration. We find that halo concentrations are independent of spin once haloes manifestly out of equilibrium are removed from the sample. Compared to their relaxed brethren, the concentrations of out-of-equilibrium haloes tend to be lower and to have more scatter, while their spins tend to be higher. A number of previously noted trends within the halo population are induced primarily by these properties of unrelaxed systems. Finally, we compare the result of predicting halo concentrations using the mass assembly history of the *main progenitor* with estimates based on simple arguments based on the assembly time of *all progenitors*. The latter typically do as well or better than the former, suggesting that halo concentration depends not only on the evolutionary path of a halo's main progenitor, but on how and when *all* of its constituents collapsed to form non-linear objects.

**Key words:** cosmology: theory, cosmology: dark matter, galaxies: haloes, methods: numerical

## 1 INTRODUCTION

The advent of large cosmological N-body simulations has enabled important progress in our understanding of the structure of dark matter haloes. As a result, over the past few years a broad consensus has emerged about the mass function of these collapsed structures, about their mass profiles and shapes, and about the presence of substructure within the vitalised region of a halo. The spherically-averaged halo

mass profiles are of particular interest, not only because of their immediate applicability to a host of observational diagnostics, such as gravitational lensing and disk galaxy rotation curves, but also because of the apparent simplicity of their structure.

Navarro, Frenk, & White (1995, 1996, 1997, hereafter NFW) argued that the density profile of a dark matter halo may be approximated by a simple formula with two free parameters;

$$\frac{\rho(r)}{\rho_{\text{crit}}} = \frac{\delta_c}{(r/r_s)(1+r/r_s)^2}, \quad (1)$$

\* E-mail: fausti@if.ufrgs.br

† Fellow of the Canadian Institute for Advanced Research

where  $\rho_{\text{crit}} = 3H_0^2/8\pi G$  is the critical density for closure<sup>1</sup>,  $\delta_c$  is a characteristic density contrast, and  $r_s$  is a scale radius. Remarkably, this formula seems to hold for essentially all haloes assembled hierarchically and close to virial equilibrium, regardless of mass and of the details of the cosmological model. The cosmological information is encoded in correlations between the parameters of the NFW profile, so that observational constraints on such parameters may be translated directly into interesting constraints on cosmological parameters.

As discussed by NFW, such correlations arise because the characteristic density of a system appears to evoke the density of the universe at a suitably defined time of collapse. This result has been revisited and confirmed by a rich literature on the topic (see, e.g. Kravtsov, Klypin, & Khokhlov 1997; Avila-Reese et al. 1999; Jing 2000; Ghigna et al. 2000; Klypin et al. 2001; Bullock et al. 2001; Eke, Navarro, & Steinmetz 2001), which has led to the development of a number of semi-analytic and empirical procedures to explain and predict the structural parameters of cold dark matter (CDM) haloes as a function of mass, redshift, and cosmological parameters. The various approaches differ in detail and lead to significantly different predictions, especially when extrapolated to halo masses or to redshifts which were not well sampled by the numerical data on which they were based.

NFW, for example, proposed that the characteristic density is set at the time when most of the mass of a halo is in non-linear, collapsed structures. Bullock et al. (2001, B01), on the other hand, argued that a better fit to their N-body results is obtained by assuming that the scale radius of haloes of fixed virial mass is independent of redshift, leading to a substantially different redshift evolution of the halo structural parameters than envisioned by NFW. This conclusion was seconded by Eke, Navarro, & Steinmetz (2001, ENS) who proposed a modification of B01's approach to take into account models with truncated power spectra, such as expected, for example, in a warm dark matter-dominated universe.

The predictions of these models also differ significantly for extremely massive haloes, but these predictions have been notoriously difficult to validate since these systems are woefully under-represented in simulations that survey a small fraction of the Hubble volume. For example, NFW argued that the characteristic density of a halo is set by the mean density of the Universe at the time of collapse. Very massive systems have, by necessity, been assembled quite recently (indeed, they are assembling *today*), and therefore they should all have similar characteristic densities. B01's model, on the other hand, defines collapse redshifts in a different way, predicting much lower concentrations for very massive objects.

Despite the (qualified) success of these models at reproducing the *average* mass and redshift dependence of halo structural parameters, they are in general unable to account for the sizable scatter about the mean relations. As first discussed by Jing (2000), a sizable spread in concentration (of

order  $\sigma_{\log_{10} c} \sim 0.1$ ) is seen at all halo masses, and a number of models have attempted to reproduce this result using semi-analytic models. Amongst the most successful are those that ascribe variations in concentration to disparities in the assembly history of haloes of given mass. For example, Wechsler et al. (2002, W02) identify the scatter with variations in the time when the rate of mass accretion onto the main progenitor peaks. A similar proposal was advanced by Zhao et al. (2003a,b, Z01), who argued that the concentration of a halo is effectively set during periods when the most massive progenitor is in a phase of fast mass accretion.

Given the disparities between models, it is important to validate their predictions in a regime different from that used to calibrate their parameters. Indeed, with few exceptions, most of these studies have explored numerically a relatively narrow range of halo mass and redshift, favouring (because they are easier to simulate) haloes with masses of the order of the characteristic non-linear mass,  $M_*$ , and redshifts close to the present day ( $z \sim 0$ ). Testing these predictions on a representative sample of haloes of mass much greater or much lower than  $M_*$ , or at very high redshift, requires either simulations of enormous dynamic range, or especially designed sets of simulations that probe various mass or redshift intervals one at a time.

One version of the latter approach was adopted by NFW, who simulated *individually* haloes spanning a large range in mass. The price paid is the relatively few haloes that can be studied using such simulation series, as well as the lingering possibility that the procedure used to select the few simulated haloes may introduce some subtle bias or artifact. Recently, Macciò et al. (2007, M07), have combined several simulations of varying mass resolution and box size in order to try and extend earlier results to  $M \ll M_*$  scales. This approach is not without pitfalls, however. For example, in order to resolve a statistically significant sample of haloes with masses as low as  $10^{10} h^{-1} M_\odot$ , M07 use a simulation box as small as  $14.2 h^{-1}$  Mpc on a side, leading to concerns that the substantial large-scale power missing from such small periodic realisation may unduly influence the results.

One way to overcome such shortcomings is to increase the dynamic range of the simulation, so as to encompass a volume large enough to be representative while at the same time having enough mass resolution to extend the analysis well below or well above  $M_*$ . This is the approach we adopt in this paper, where we use the *Millennium Simulation* (MS) to address these issues. The enormous volume of the MS ( $500^3 h^{-3}$  Mpc<sup>3</sup>), combined with the vast number of particles ( $2160^3$ ), make this simulation ideal to characterise, with minimal statistical uncertainty, the dependence of the structural parameters of  $\Lambda$ CDM haloes on mass, spin, formation time, and departures from equilibrium. We extend and check our MS results at low masses by using an additional large simulation of a  $100 h^{-1}$  Mpc region with about 10 times better mass resolution.

For reasons discussed in detail below, numerical limitations impose a lower mass limit of about  $10^{12} h^{-1} M_\odot$  in our analysis. Thus, our study does not extend to halo masses as low as those probed by M07 (whose smallest box is filled with particles of mass  $1.4 \times 10^7 h^{-1} M_\odot$ ), but is aimed at extending previous work to give reliable and statistically robust results for large and representative samples of haloes over

<sup>1</sup> We express the present-day value of Hubble's constant as  $H_0 = 100 h \text{ km s}^{-1} \text{ Mpc}^{-1}$ .

the full range from  $10^{12}$  to  $10^{15} h^{-1} M_{\odot}$ . The large number of haloes in the *MS* also allows us to study in detail deviations from the mean trends and, in particular, the possible presence of systems with unusual properties, such as clusters with unusually high concentrations or galaxy haloes of unusually low density. In this paper we concentrate on the properties of haloes at  $z = 0$ . A second paper will extend these results to high redshift.

The plan for this paper is as follows. We describe briefly the simulation and the halo identification technique in Section 2. After a brief introduction to the *MS* (Section 2.1) we describe our halo identification (Section 2.2) and selection (Section 2.3) techniques. We also describe the merger trees in Section 2.4 and the NFW profile fitting procedure in Section 2.5. The dependence of the halo structural parameters on mass, spin, and formation time, as well as the performance of various semi-analytic models designed to predict halo concentrations, are discussed in Section 3. We conclude with a brief summary in Section 4.

## 2 HALOES IN THE MILLENNIUM SIMULATION

Our analysis is mainly based on haloes identified in the *Millennium Simulation (MS)*, (Springel et al. 2005a), and in this section we describe briefly our halo identification and cataloguing procedure. For completeness, we begin with a brief summary of the main characteristics of the *MS*, and then move on to a fairly detailed characterisation of the halo sample. Readers less interested in these technical details may wish to gloss over this section and skip to Section 3, where our main results are presented and discussed.

### 2.1 The simulations

The *Millennium Simulation* is a large N-body simulation of the concordance  $\Lambda$ CDM cosmogony. It follows  $N = 2160^3$  particles in a periodic box of  $L_{\text{box}} = 500 h^{-1} \text{Mpc}$  on a side. The cosmological parameters were chosen to be consistent with a combined analysis of the 2dFGRS (Colless et al. 2001; Percival et al. 2001) and first year WMAP data (Spergel et al. 2003). They are  $\Omega_{\text{m}} = \Omega_{\text{dm}} + \Omega_{\text{b}} = 0.25$ ,  $\Omega_{\text{b}} = 0.045$ ,  $h = 0.73$ ,  $\Omega_{\Lambda} = 0.75$ ,  $n = 1$ , and  $\sigma_8 = 0.9$ . Here  $\Omega$  denotes the present day contribution of each component to the matter-energy density of the Universe, expressed in units of the critical density for closure,  $\rho_{\text{crit}}$ ;  $n$  is the spectral index of the primordial density fluctuations, and  $\sigma_8$  is the linear rms mass fluctuations in  $8h^{-1} \text{Mpc}$  spheres at  $z = 0$ . Compared with the parameter values now favoured by the three-year WMAP analysis (Spergel et al. 2006), the main differences are that a modest tilt,  $n = 0.95 \pm 0.02$  and a lower  $\sigma_8 = 0.74 \pm 0.05$  are favoured by the analysis of these latest data.

With our choice of cosmological parameters, the particle mass in the *MS* is  $8.6 \times 10^8 h^{-1} M_{\odot}$ . Particle pairwise interactions are softened on scales smaller than (Plummer-equivalent)  $\epsilon = 5 h^{-1} \text{kpc}$ . Since galaxy-sized haloes ( $M \sim 10^{12} h^{-1} M_{\odot}$ ) in the *MS* are represented with only about 1000 particles, we have verified that our results are insensitive to numerical resolution by comparing them with a second simulation of a smaller volume,  $L_{\text{box}} = 100 h^{-1} \text{Mpc}$ , but

of 9 times higher mass resolution. This simulation adopted the same cosmological model as the *MS*, and evolved  $N = 900^3$  particles of mass  $9.5 \times 10^7 h^{-1} M_{\odot}$ , softened on scales smaller than  $\epsilon = 2.4 h^{-1} \text{kpc}$ .

Both simulations were performed with a special version of the GADGET-2 code (Springel 2005b) that was specially designed for massively parallel computation and for low memory consumption, a prerequisite for a simulation of the size and computational cost of the *MS*.

### 2.2 Halo identification

The simulation code produced on the fly a *friends of friends* (Davis et al. 1985) (FOF) group catalogue with link parameter,  $b = 0.2$ , and at least 20 particles per group. At  $z = 0$ , this procedure identifies  $1.77 \times 10^6$  groups in the *MS*. We have also used SUBFIND, the *subhalo finder* algorithm described in Springel et al. (2001), in order to clean up the group catalogue of loosely-bound FOF structures, and to analyse the substructure within each halo (see Sec. 2.3).

Like FOF, SUBFIND keeps only substructures containing 20 or more particles. In this way, each FOF halo is decomposed into a *background halo* (or the most massive “substructure”) and zero or more embedded substructures. In the *MS*, SUBFIND finds at  $z = 0$  a total of  $1.82 \times 10^7$  substructures, with the largest FOF group containing 2328 of them.

#### 2.2.1 Halo centring

Since much of our analysis deals with radial profiles, it is important to define carefully the centre of a halo. We choose the position,  $\mathbf{r}_c$ , of the particle with minimum gravitational potential in the most massive substructure (the potential centre). Although this seems like a sensible choice, it is important to check that other plausible options do not lead to large differences in the location of the halo centre.

We have therefore compared the potential centre with the result of the “shrinking sphere” algorithm (Power et al. 2003), which is intended to converge towards the density maximum of the most massive substructure, independent of the SUBFIND algorithm. It starts by enclosing all FOF particles within a sphere and computes iteratively their centre of mass, shrinking the radius of the sphere by  $r_i = r_0(1 - 0.025)^i$ , and rejecting particles outside the sphere. The iteration stops when the shrinking sphere contains 1% of the initial number of particles.

We carried out this comparison in a sub-volume of the *MS* containing 2000 haloes with  $N_{\text{FOF}} > 450$ . For 93% of these haloes the methods agree in the centre position, with a difference smaller than the gravitational softening,  $\epsilon$ . However, we note that the result can depend on the geometry of the FOF group. When the FOF halo is double (or multiple) and its centre of mass is far from the centre of the most massive substructure, the shrinking sphere may converge to another slightly less massive substructure. We conclude that the potential centre is a more robust determination of the halo centre, but that the discrepancy between the two methods could be used to flag problematic haloes whose mass distributions deviate significantly from spherical symmetry.

### 2.2.2 Halo boundary

Using the potential centre, we define the limiting radius  $r_{\text{lim}}$  of a halo by the radius that contains a specified density contrast  $\bar{\rho}(r) = \Delta \rho_{\text{crit}}$ . This defines implicitly an associated mass for the halo through

$$M = \frac{4}{3}\pi\Delta\rho_{\text{crit}}r_{\text{lim}}^3. \quad (2)$$

We note that this includes all the particles inside this spherical volume, and not only the particles grouped by the FOF or the SUBFIND algorithms.

The choice of  $\Delta$  varies in the literature, with some authors using a fixed value, such as NFW, who adopted  $\Delta = 200$ , and others, such as B01, who choose a value motivated by the spherical collapse model, where  $\Delta \sim 178 \Omega_m^{0.45}$  (for a flat universe), which gives  $\Delta = 95.4$  at  $z = 0$  for our adopted  $\Lambda$ CDM parameters (e.g. Lahav et al. 1991; Eke, Cole, & Frenk 1996). The drawback of the latter choice is its dependence on redshift and cosmological parameters. We keep track of *both* definitions in our halo catalogue, but will quote mainly values adopting  $\Delta = 200$ . When necessary, we shall specify the choice by a subscript; e.g.,  $M_{200}$  and  $r_{200}$  are the mass and radius of a halo adopting  $\Delta = 200$ ;  $M_{\text{vir}}$  and  $r_{\text{vir}}$  correspond to adopting  $\Delta = 95.4$ . Unless otherwise specified, quantities listed without subscript throughout the paper assume  $\Delta = 200$ .

### 2.3 Halo selection

Dark matter haloes are dynamic structures, constantly accreting material and often substantially out of virial equilibrium. In these circumstances, haloes evolve quickly, so that the parameters used to specify their properties change rapidly and are thus ill-defined. Furthermore, in the case of an ongoing major merger, even the definition of the halo centre becomes ambiguous, so that the characterisation of a system by spherically-averaged profiles is of little use. As we shall see below, departures from equilibrium not only add to the scatter in the correlations that we seek to establish, but can also bias the resulting trends, unless care is taken to identify and correct for the effect of these transient structures.

#### 2.3.1 Relaxed and unrelaxed haloes

The equilibrium state of each halo is assessed by means of three objective criteria:

i) **Substructure mass fraction:** We compute the mass fraction in resolved substructures whose centres lie inside  $r_{\text{vir}}$ :  $f_{\text{sub}} = \sum_{i \neq 0}^{N_{\text{sub}}} M_{\text{sub},i} / M_{\text{vir}}$ . Note that in this definition  $f_{\text{sub}}$  does not include the most massive substructure as this is simply the bound component of the main halo.

ii) **Centre of mass displacement:** We define  $s$ , the normalised offset between the centre of mass of the halo (computed using all particles within  $r_{\text{vir}}$ ) and the potential centre, as  $s = |\mathbf{r}_c - \mathbf{r}_{\text{cm}}| / r_{\text{vir}}$  (Thomas et al. 2001).

iii) **Virial ratio:** We compute  $2T/|U|$ , where  $T$  is the total kinetic energy of the halo particles within  $r_{\text{vir}}$  and  $U$  their gravitational self potential energy. To estimate  $U$ , we use a random sample of 1000 particles when  $N_i \geq 1000$ . We obtain physical velocities with respect to the potential centre by

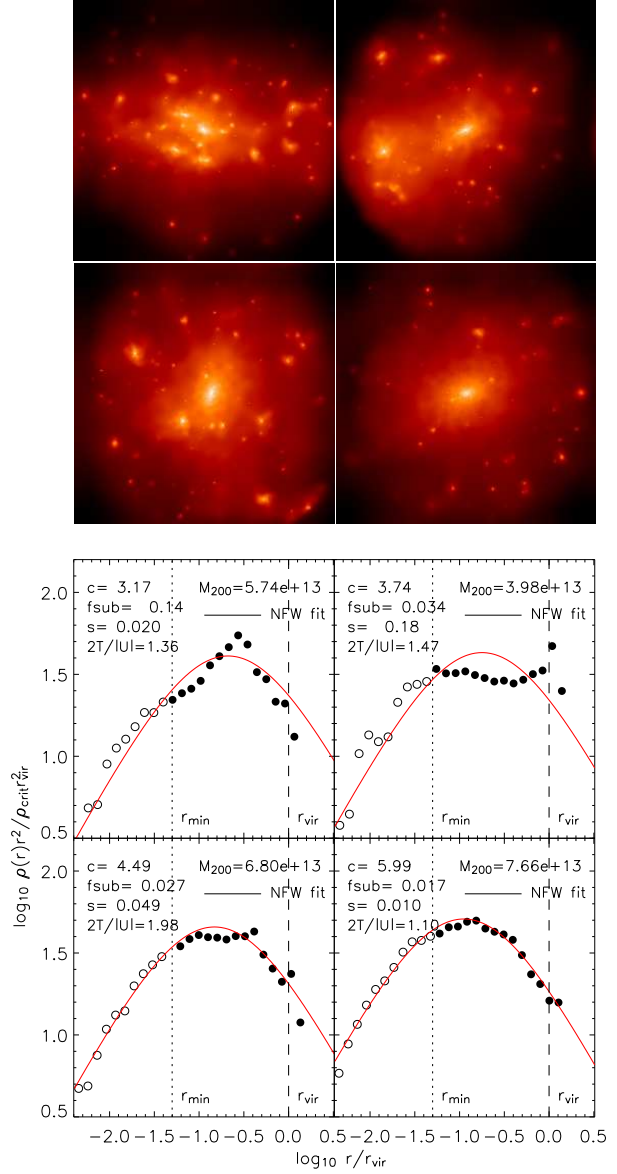


**Figure 1.** Images (top) and corresponding spherically averaged density profiles (bottom) in four haloes of similar mass. The halo shown in the lower right panel of each set satisfies all our selection criteria and is, therefore, close to dynamical equilibrium. Note that the NFW profile (solid line) provides an excellent fit to this halo. The halo mass, concentration and the values of the three quantities,  $f_{\text{sub}}$ ,  $s$  and  $2T/|U|$  used in the selection are given in the legend. The NFW fitting procedure, which here is performed only over the indicated range  $r_{\text{min}} < r < r_{\text{vir}}$ , is described in Section 2.5. The remaining three haloes are excluded from our *relaxed* sample as they fail at least one of the selection criteria. The halo on the upper left has a large amount of substructure,  $f_{\text{sub}} > 0.1$ . The one in the upper right panel is undergoing a major merger. Note that the merging partner does not contribute to  $f_{\text{sub}}$ , since its centre lies outside the virial radius, but some of its associated material displaces the centre of mass of the system, resulting in  $s > 0.07$ . The halo in the lower left panel satisfies these two criteria, but has  $2T/|U| > 1.35$ . The corresponding panels in the lower plot show that these unrelaxed haloes have density profiles that are clearly not well described by NFW profiles.

adding the Hubble flow to the peculiar velocities and then we compute the halo kinetic energy after subtracting from the velocities the motion of the halo centre of mass.

Fig. 1 shows images and spherically averaged density profiles for a set of three haloes of similar mass that are rejected by just one of each of the above criteria. Systems such as the one shown in the top-left panel (large  $f_{\text{sub}}$ ) are clearly not relaxed and it is not surprising that the large number of substructures affect halo properties such as concentration, angular momentum and shape (Gao et al. 2004; Shaw et al. 2005). Note that, despite the large value of  $f_{\text{sub}}$ , the centre of mass displacement is quite small, since the spatial distribution of substructures happens to be fairly symmetric.

Conversely, the halo shown in the upper-right panel of Fig. 1 has small  $f_{\text{sub}}$ , but is rejected by our cut on the centre of mass offset  $s$ . This is clearly an ongoing merger where, because the merging partner of the main halo lies just outside the virial radius, it contributes little to  $f_{\text{sub}}$ . Thus the  $s$  criterion is complementary to  $f_{\text{sub}}$ . This is important, because the ability of SUBFIND to detect self-bound substructures is heavily resolution-dependent:  $f_{\text{sub}}$  is likely to be substantially underestimated in low-mass haloes resolved with few particles.

These two criteria, however, make no use of kinematic information and so our third criterion, based on  $2T/|U|$ , is a useful supplement able to reject haloes that, despite passing the other two conditions, are far from dynamical equilibrium. This is especially the case for ongoing mergers and artificially linked haloes. An example of a halo rejected by just this criterion is shown in the lower-left panel of Fig. 1.

Finally, the lower-right panel of Fig. 1 shows an example of a halo that makes it into our *relaxed* sample. These relaxed haloes generally have smooth density profiles and are well fitted by NFW profiles.

### 2.3.2 $N$ -dependence of selection criteria

Fig. 2 shows the various correlations between the criteria used to identify “relaxed” haloes ( $f_{\text{sub}}$ ,  $s$  and  $2T/|U|$ ) and the number of particles within the virial radius. Note that the equilibrium measures we use do not have bimodal distributions, but, instead, are roughly continuous, with extended tails. This reflects the fact that haloes assemble hierarchically: all haloes are in the process of accreting some material and are, therefore, to some extent unrelaxed. (Note for example, that the median  $2T/|U|$  is slightly greater than unity, as reported in earlier work (see, e.g. Cole & Lacey 1996)). Thus, our selection criteria just provide a simple, but somewhat arbitrary, way of trimming off the tail of worst offenders, typically ongoing mergers.

The shaded regions in Fig. 2 show the areas of parameter space rejected by our criteria to select *relaxed* haloes:  $f_{\text{sub}} < 0.1$ ,  $s < 0.07$  and  $2T/|U| < 1.35$ . The top-right panel shows the expected strong correlation between our measures of asymmetry and lumpiness, as well as how the tail of high  $s$  and high  $f_{\text{sub}}$  values is removed by the selection.

Of all the selection criteria, the one most sensitive to the number of particles in the halo is  $f_{\text{sub}}$ . This is clearly seen in the top-left panel of Fig. 2, where the stepped line shows, as a function of  $N_{\text{vir}}$ , the fraction of haloes with no resolved substructures, i.e.,  $f_{\text{sub}} = 0$ . This rises quickly

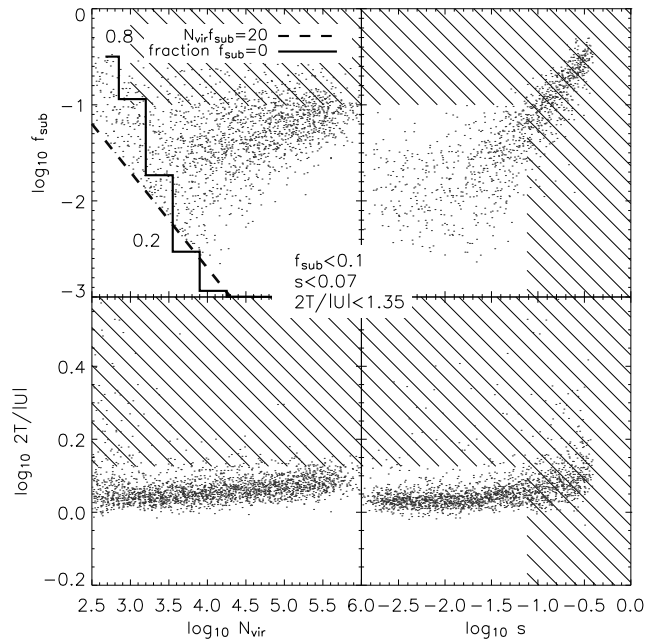


**Figure 2.** The various criteria used to define our *relaxed* sample of haloes (see Section 2.3 for definitions), shown as a function of the number of particles within the virial radius. Shaded regions indicate the location of “unrelaxed” haloes. The dots sample uniformly all MS haloes with  $N_{\text{vir}} > 300$  in each plot. *Top left:* The fraction of halo mass in resolved substructures,  $f_{\text{sub}}$  vs. the number of particles in the halo  $N$ . The dashed line shows the detection limit of SUBFIND,  $N_{\text{min}} = 20/N$ . The solid stepped line shows the fraction of haloes with no resolved substructures in each mass bin (i.e., those with  $f_{\text{sub}} = 0$ ). *Top right:* The centre of mass offset  $s$  vs the substructure fraction  $f_{\text{sub}}$ . The criteria  $f_{\text{sub}} < 0.1$  and  $s < 0.07$  reject the tail of haloes with high  $f_{\text{sub}}$  and  $s$ . *Bottom:* The criterion  $2T/|U| < 1.35$  is intended to reject haloes far from dynamical equilibrium.

with decreasing  $N_{\text{vir}}$ , so that more than 80% of haloes with  $300 < N_{\text{vir}} < 1000$  particles have no discernible substructures. By contrast, essentially *all* haloes with more than 10,000 particles have at least one massive subhalo within the virial radius.

A significant fraction of haloes with fewer than 1000 particles also have very large values of the virial ratio  $2T/|U|$ , as shown in the bottom-left panel of Fig. 2. As discussed by Bett et al. (2007), these are loosely bound objects connected by a tenuous bridge of particles, or objects lying in the periphery of much more massive systems that owe their large kinetic energy to contamination with fast-moving members of the other system.

These results suggest that a minimum number of particles may also be required in order to obtain robust results independent of numerical artifact. We shall see below that about  $\sim 1000$  particles or more are needed in order to avoid biases when deriving structural parameters from fits to the halo mass profiles.

The fraction of haloes rejected by these cuts varies slowly with mass, rising from 20% at  $M_{\text{vir}} = 10^{12} h^{-1} M_{\odot}$  to 50% at  $M_{\text{vir}} = 10^{15} h^{-1} M_{\odot}$  (see numbers given in Fig. 6 and Table 1). The criterion  $s < 0.07$  rejects the most haloes; a

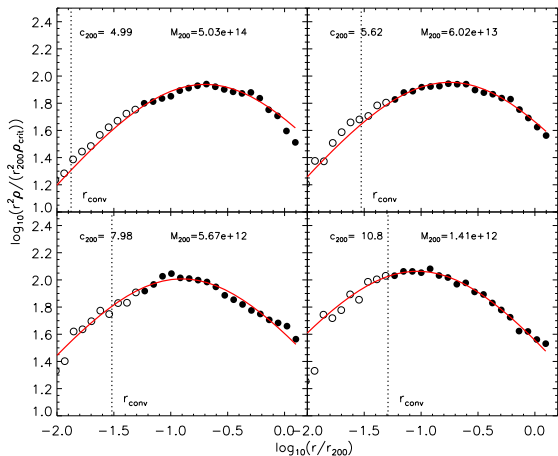


**Figure 3.** Density profiles,  $r^2\rho(r)$ , and least squares NFW fits for four *relaxed* haloes. The fits are performed over the radial range  $0.05 < r/r_{\text{vir}} < 1$ , shown by the solid circles, and extend slightly beyond  $r_{200}$ . The vertical line marks the position of the mass profile convergence radius derived by Power et al (2003). This is always smaller than the minimum fit radius,  $0.05 r_{\text{vir}}$ .

smaller but significant fraction of haloes that pass that cut are removed by the  $f_{\text{sub}} < 0.1$  criterion; while only a few additional haloes are rejected by the  $2T/|U| < 1.35$  test.

## 2.4 Merger trees and formation times

We use the merger trees for the *MS* described in detail by Harker et al. (2006) and Bower et al. (2006). These differ slightly from those used by Springel (2005b), but the differences are only significant for haloes undergoing major mergers, which would not pass the stringent selection criteria listed above. At each of the approximately 60 output redshifts of the simulation, the merger tree provides us with a list of all the haloes that will subsequently merge to become part of the final halo. We exploit this information below in order to investigate the dependence of halo concentration on formation history (see Section 3.4).

## 2.5 Profile fitting

For each halo identified using the procedure outlined in Section 2.2 we have computed a spherically-averaged density profile by binning the halo mass in equally spaced bins in  $\log_{10}(r)$ , between the virial radius and  $\log_{10}(r/r_{\text{vir}}) = -2.5$ . After extensive testing, we concluded that using 32 bins, corresponding to  $\Delta \log_{10}(r) = -0.078$ , is enough to produce robust and unbiased results.

The density profiles of four *relaxed* haloes are shown in Fig. 3, together with fits using the NFW profile (eq. 1). This profile has two free parameters,  $\delta_c$  and  $r_s$ , which are both adjusted to minimise the rms deviation,  $\sigma_{\text{fit}}$ , between the binned  $\rho(r)$  and the NFW profile,

$$\sigma_{\text{fit}}^2 = \frac{1}{N_{\text{bins}} - 1} \sum_{i=1}^{N_{\text{bins}}} \left[ \log_{10} \rho_i - \log_{10} \rho_{\text{NFW}}(\delta_c; r_s) \right]^2. \quad (3)$$

Note that eq. 3 assigns equal weight to each bin. We have

explicitly checked that none of our results varies significantly if we adopt other plausible choices, such as Poisson weighting each bin (for further discussion, see Jing (2000)).

Once the parameters  $\delta_c$  and  $r_s$  for each halo are retrieved from the fitting procedure, they may be expressed in a variety of forms. In order to be consistent with the original NFW work, we choose to express the results in terms of a mass,  $M_{200}$ , and a concentration,  $c = c_{200} = r_{200}/r_s$ , that result from adopting  $\Delta = 200$  in the definition of the virial properties of a halo (eq. 2).

The radial range adopted for the fitting procedure is important, especially since haloes of different mass are resolved to varying degree in a single cosmological simulation. After experimenting at length, and especially after comparing the fit parameters obtained in the overlapping mass range of the two simulations (Section 2.1), we settled on carrying out the fits over a uniform radial range (in virial units). This ensures that all haloes, regardless of mass, are treated equally, minimising the possibility of introducing subtle mass-dependent biases in the analysis.

Fig 4 shows the mass-concentration dependence obtained for the *MS* (symbols) and the higher mass resolution simulation (lines) for four different choices of the radial range. The symbols and lines extend down to haloes with  $\sim 1000$  particles within the virial radius in each case and indicate the median (solid circles and lines) as well as the 20 and 80 percentiles of the distribution. To guide the comparison, the dotted line shows a power law,  $c \propto M_{200}^{-1/10}$ , and is the same in all panels.

Note that, provided the minimum radius is  $\geq 0.05 r_{\text{vir}}$ , the fit parameters appear to depend only weakly on the radial range, but that the distribution of concentrations is narrowest for  $0.05 < r/r_{\text{vir}} < 1$ . For this choice (which we adopt hereafter in our analysis) there is also good agreement between the two simulations on mass scales probed in both with at least 1000 particles.

However, as shown in Fig. 5, the mean quality of the fits, as measured by  $\sigma_{\text{fit}}$ , deteriorates noticeably for haloes with less than 10,000 particles as a result of the relatively small number of particles per bin. Although this does not seem to introduce a bias in the mass-concentration relation, we have decided to retain, conservatively, only haloes with  $N > 10,000$  for our analysis, and to combine the two simulations in order to probe the halo mass range  $10^{12} < M/h^{-1}M_{\odot} < 10^{15}$ .

Finally, we considered a couple of alternative methods for characterising the halo concentration that do not assume an NFW density profile, such as the ratio of maximum to virial circular velocities,  $V_{\text{max}}/V_{\text{vir}}$  (Gao et al. 2004) or the ratio of masses enclosing different overdensities, such as  $M_{\text{vir}}/M_{1000}$  (Thomas et al. 2001). These measures of the concentration, presumably because they use information on just two particular points in the profile, lead to substantially larger scatter in the correlations that we examine here, so we do not consider them further in this paper.

## 3 RESULTS AND DISCUSSION

### 3.1 Concentration vs mass

Fig. 6 shows concentration as a function of halo mass for all haloes selected following the procedure described above.

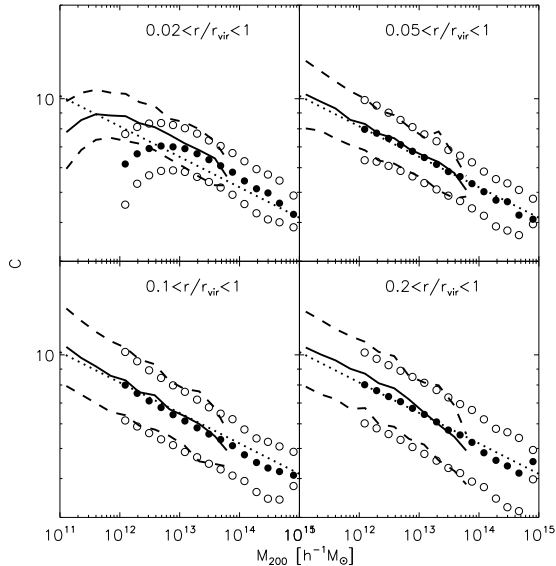


**Figure 4.** The median, 20 and 80 percentiles of the concentration,  $c_{200}$ , as a function of halo mass,  $M_{200}$ . The symbols extending to high masses show the results from the MS while the overlapping set of solid and dotted lines extending to lower masses show the results from a simulation with  $9\times$  higher mass resolution. Each panel corresponds to a different radial range adopted for the fits. Data for each simulation are shown for haloes with  $N > 1000$  particles, corresponding to  $\sim 10^{12} h^{-1} M_{\odot}$  in the MS. The dotted line shows a power law,  $c \propto M^{-1/10}$ , and is the same in all panels.

The upper panel is for our *relaxed* halo sample, while the lower panel show results for the complete sample, including systems that do not meet our equilibrium criteria.

In both samples, the correlation between mass and concentration is well defined, but rather weak. A power-law fits the median concentration as a function of mass fairly well; we find:

$$c_{200} = 5.26 \left( M_{200}/10^{14} h^{-1} M_{\odot} \right)^{-0.10}, \quad (4)$$

for *relaxed* haloes, and

$$c_{200} = 4.67 \left( M_{200}/10^{14} h^{-1} M_{\odot} \right)^{-0.11} \quad (5)$$

for the complete halo sample.

Our power-law fit is in good agreement with the results of M07, who find  $c_{200} \sim 5.6 (M_{200}/10^{14} h^{-1} M_{\odot})^{-0.098}$  for the *average* concentration of their sample of relaxed haloes. These authors also report that concentrations are systematically lower when considering the full sample of haloes. The small difference between our results and M07's may be due to variations between mean and median, as well as on the different criteria used to construct the relaxed halo sample. Nevertheless, the agreement in the exponent of the power-law is remarkable, especially considering that these authors explore a mass range different from ours, namely  $2 \times 10^9 < M_{200}/h^{-1} M_{\odot} < 2 \times 10^{13}$ . Combining these results with ours, we conclude that *a single power law fits the concentration-mass dependence for about six decades in mass.*

Over the mass range covered by our simulations the concentration-mass dependence is in reasonable agreement with the predictions of NFW and of ENS, as shown, re-

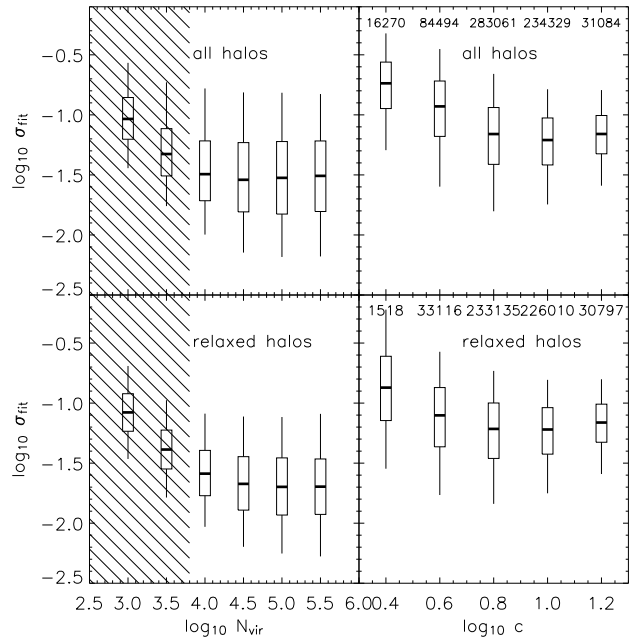


**Figure 5.** The dependence of the rms residual deviation,  $\sigma_{\text{fit}}$ , about the best-fitting NFW density profile on the number of particles per halo and on halo concentration. The boxes show the medians and the 25% and 75% centiles of the distribution, while the whiskers show the 5% and 95% tails. The numbers along the top of each panel indicate the number of haloes within each bin. Top panels include all MS haloes with  $N_{\text{vir}} > 450$  as no other selection criteria have been applied. The upturn in  $\sigma_{\text{fit}}$  for low-concentration relaxed haloes is due to the inclusion of haloes with less than 10,000 particles. This upturn disappears once the  $N > 10,000$  criterion is imposed.

spectively, by the dotted and dashed lines in Fig. 6<sup>2</sup>. The agreement, however, is not perfect, and both models appear to underestimate somewhat the median concentration at the low mass end.

At the high-mass end, where there is a hint that concentrations are approaching a constant value, the NFW model does slightly better than ENS. This is because a constant concentration for very massive objects is implicit in the NFW model, but not in ENS nor in the model of B01, which is shown by a dot-dashed line in Fig. 6. Both ENS and B01 predict a strong decline in concentration at the very high mass end. For the parameters favoured by B01, the disagreement for  $M > 10^{13.5} h^{-1} M_{\odot}$  is dramatic, and cautions, as already pointed out by Zhao et al. (2003b), against using this model for predicting the concentrations of massive haloes.

Finally, we note that M07 argue that the B01 model reproduces their results better than ENS for haloes of mass a few times  $10^9 h^{-1} M_{\odot}$ . However, the differences between the two models only become appreciable below  $\sim 10^{10} h^{-1} M_{\odot}$ , which corresponds to only about 700 particles in their highest-resolution simulation. Given (i) the large scatter in

<sup>2</sup> These predictions use the original parameters in those papers and have not been adjusted further, except for adopting the power-spectrum “shape” parameter,  $\Gamma = 0.15$ , as the best match to the power spectrum adopted for the MS.

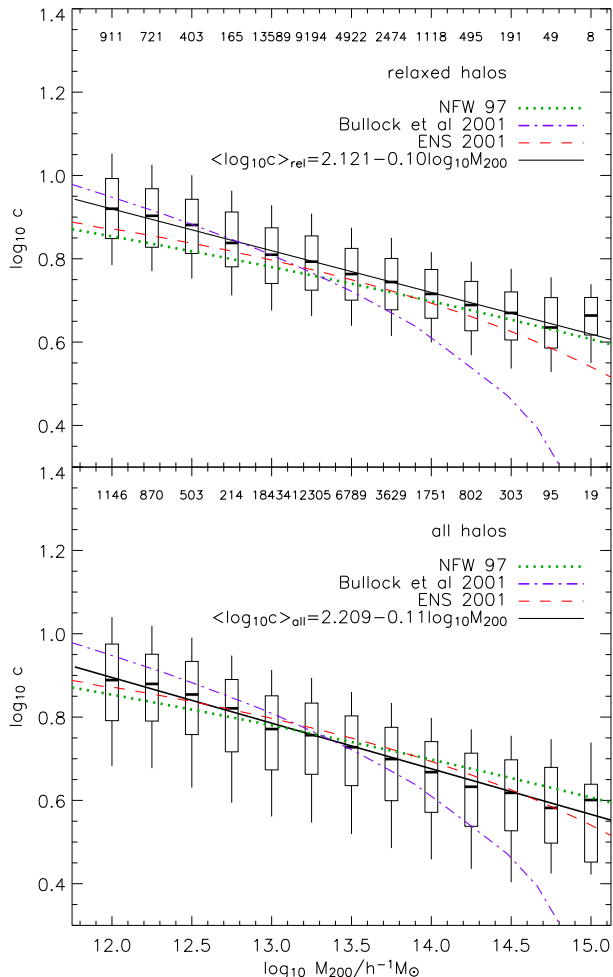


**Figure 6.** Mass-concentration relation for *relaxed* haloes (top panel) and for all haloes (bottom panel). The boxes represent the 25% and 75% centiles of the distribution, while the whiskers show the 5% and 95% tails. The numbers on the top of each panel indicate the number of haloes in each mass bin. The median concentration as a function of mass is shown by the solid line and is well fit by the linear relations given in the legend of each panel. The dot-dashed line shows the prediction of the Bullock et al. (2001) model (using  $c_{\text{vir}}2.f$  available from the authors); the dashed and dotted lines corresponds to the Eke, Navarro, & Steinmetz (2001) and NFW models, respectively, with  $\Gamma = 0.15$ , as this approximates best the input power spectrum of the *MS*. See text for further details.

the correlation; (ii) our finding that at least 1000 particles are needed to produce unbiased results, and (iii) the worries expressed in Section 1 about the rather small box used by M07 to resolve low-mass haloes, we conclude that it would be premature to judge conclusively on the superiority of one model over the other at the low mass end. More definitive tests are likely to come either from much higher resolution simulations or from extending this analysis to higher redshifts, where the two models predict different behaviour. This is a topic that we intend to address in a forthcoming paper (Gao et al. 2007, in preparation).

### 3.1.1 Scatter

The large volume covered by the *MS* means that we have a large number of haloes in our sample, even in the most massive bins of Fig. 6, corresponding to rare, very massive objects with masses approaching  $10^{15} h^{-1} M_{\odot}$ . We use this to check the common assumption that, at given halo mass, concentrations are distributed following a lognormal distribution (Jing 2000).

We examine this in Fig. 7, where we show the distribution of concentrations in two mass bins. In each panel the top histogram corresponds to *all* haloes in our sample, and the lower histogram only to those deemed *relaxed* by the criteria listed in Section 2.3.

Although the overall distribution is *not* approximated well by a lognormal function, that of *relaxed* haloes is. The thick lines in Fig. 7 show fits of the form

$$P(\log_{10} c) = \frac{1}{\sigma\sqrt{2\pi}} \exp\left[-\frac{1}{2}\left(\frac{\log_{10} c - \langle \log_{10} c \rangle}{\sigma}\right)^2\right], \quad (6)$$

which is clearly a good approximation for the concentration distribution of relaxed haloes.

Intriguingly, the concentration distribution of “unrelaxed” haloes may also be approximated by a lognormal distribution, albeit of smaller mean and larger dispersion, as shown by the dotted curves in Fig. 7. The sum of the two lognormals (shown with dashed lines) is indeed a very good approximation to the overall distribution. We list the median concentration and dispersion of these distributions, as well as the fraction of “unrelaxed” haloes, as a function of mass in Table 1.

Upon inspection, a weak but systematic trend is apparent in Table 1: the *dispersion* in concentration appears to decrease monotonically as a function of mass (see also the bottom panel of Fig 8). This suggests that massive haloes are somehow a more homogeneous population than their lower mass counterparts, and may reflect the fact that massive haloes are rare objects that have collapsed recently, whereas less massive systems have a much wider distribution of assembly redshifts. We shall return to this topic below.

One may apply the distributions shown in Fig 7 to estimate the abundance of relatively rare objects. These might be, for example, massive cluster haloes of unusually *high* concentration that stand out in X-ray or lensing surveys, or perhaps galaxy-sized haloes of unusually *low* concentration which may be notable because of peculiarities in the rotation curves of the galaxies they may host.

We show this in the top and middle panels of Fig. 8, where the “plus” signs denote the fraction of haloes in each mass bin that have  $c < 4.5$ . The diamond symbols, on the other hand, indicate the fraction of systems with concentrations *exceeding* 7.5. For example, we find that slightly more than 1% of *relaxed* haloes with  $M_{200} \sim 3 \times 10^{14} h^{-1} M_{\odot}$  have  $c > 7.5$ , or about 4 objects in our  $500^3 h^{-3} \text{Mpc}^3$  volume. So clusters such as Abell 1689, for which Limousin et al. (2006) estimate  $c_{200} = 7.6$  should not be very abundant in the local Universe. Finding, through lensing or X-ray studies, many clusters as massive and as concentrated as Abell 1689 would yield strong constraints on the viability of  $\Lambda\text{CDM}$  as a cosmological model.



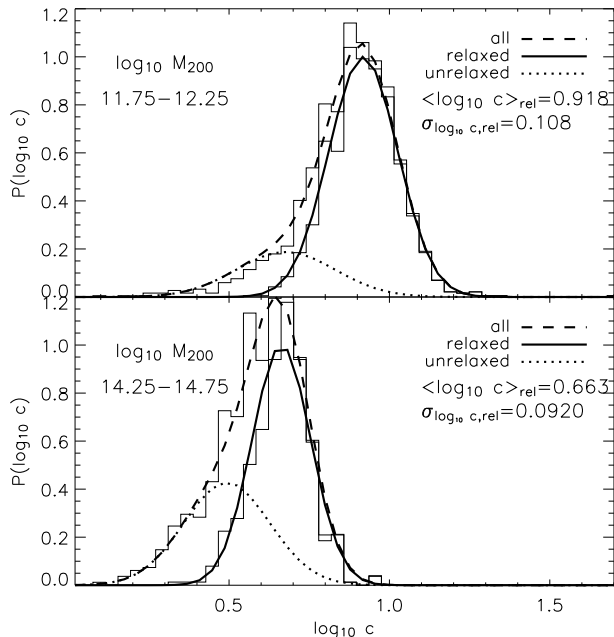


**Figure 7.** The distribution of concentrations for haloes in two different mass bins:  $11.75 < \log_{10} M_{200}/h^{-1} M_{\odot} < 12.25$  (top panel) and  $14.25 < \log_{10} M_{200}/h^{-1} M_{\odot} < 14.75$  (bottom panel). The top histogram in each panel shows the distribution for all haloes, the lower histogram that corresponding to the *relaxed* halo sample. The smooth curves are lognormal fits. Note that the overall distribution may be very well approximated by the sum of two lognormal functions with parameters listed in Table 1.

### 3.2 Concentration vs spin

Although models such as those proposed by NFW, B01 or ENS may more or less account for the weak correlation between mass and concentration, they say little about the origin of the sizable scatter about the mean trend. As shown in Fig. 7, haloes of given mass have concentrations that may differ by up to a factor of three or more. What is the origin of this large scatter?

One possibility is that concentration may be related to the angular momentum of the halo and that the large scatter in the spin parameter at given mass (see, e.g., Bett et al. (2007) and references therein) is somehow related to the spread in concentration. This was explored by NFW and B01, who concluded that there was no obvious correlation between spin and concentration; however, Bailin et al. (2005) have recently argued that such correlation indeed exists, and speculate that this may explain why low surface-brightness galaxies (LSBs) appear to inhabit low-density haloes (de Blok, Bosma, & McGaugh 2003; McGaugh, Barker, & de Blok 2003).

We revisit this issue in Fig. 9, where we show the spin parameter  $\lambda = J|E|^{1/2}/GM^{5/2}$  (where  $J$  is the angular momentum with respect the potential centre and  $E$  is the binding energy of the halo) versus concentration for our full halo sample (top panel) and for *relaxed* haloes (bottom panel). Although the full halo sample shows a well-defined tail of low-concentration, fast-spinning haloes reminiscent of

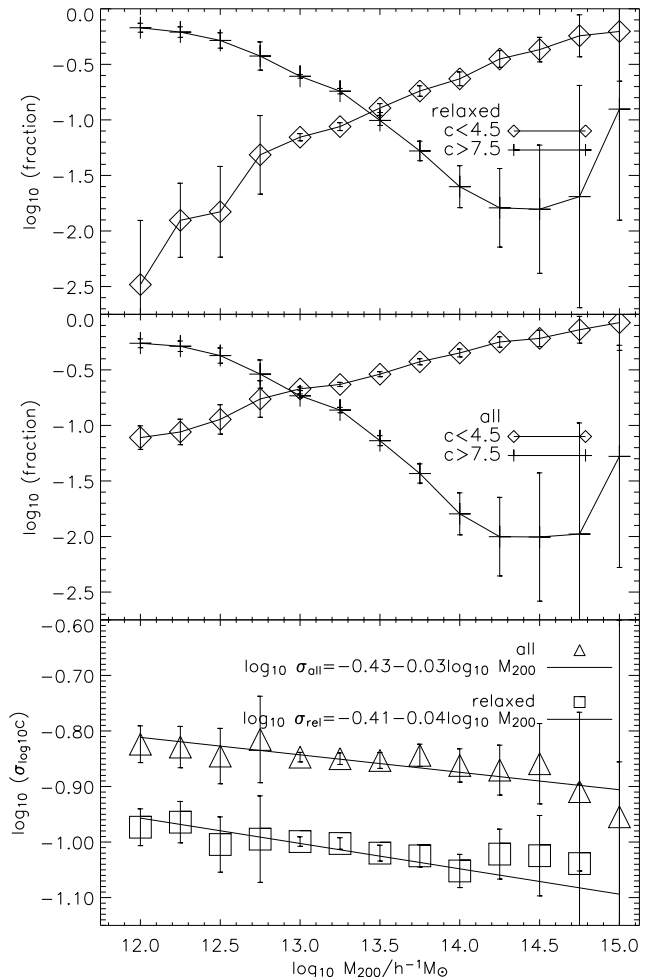


**Figure 8.** The fraction of *relaxed* haloes (top panel) and *all* haloes (middle panel) with  $c < 7.5$  (plus sign symbols) and  $c > 4.5$  (diamond-like symbols). The points connected by solid lines are the direct measurements, in mass bins. Error bars denote  $1/\sqrt{N}$  uncertainties. The lower panel shows the measured rms scatter in  $\log_{10} c$  for *all* and *relaxed* haloes, respectively.

Bailin et al.'s claim, this essentially disappears when *relaxed* haloes are considered.

As discussed above, the low concentrations of unrelaxed haloes measured by profile-fitting algorithms are a transient result of the rapidly evolving mass distribution that accompanies an accretion event, and do *not* indicate a halo with lower-than-average density.

However, this observation does not explain why, as is apparent from Fig. 9, unrelaxed systems also tend to have, on average, higher spins than their relaxed counterparts. As argued recently by D'Onghia & Navarro (2007), this is likely due to the redistribution of mass and angular momentum that occurs during mergers, combined with the arbitrary virial boundaries used to define a halo and to compute its spin. Accretion events bring mass and angular momentum into a system, but redistribute it in such a way that high-angular momentum material ends up preferentially on weakly bound orbits that may take it beyond the nominal virial radius, thereby reducing  $\lambda$ . This effect seems to be par-

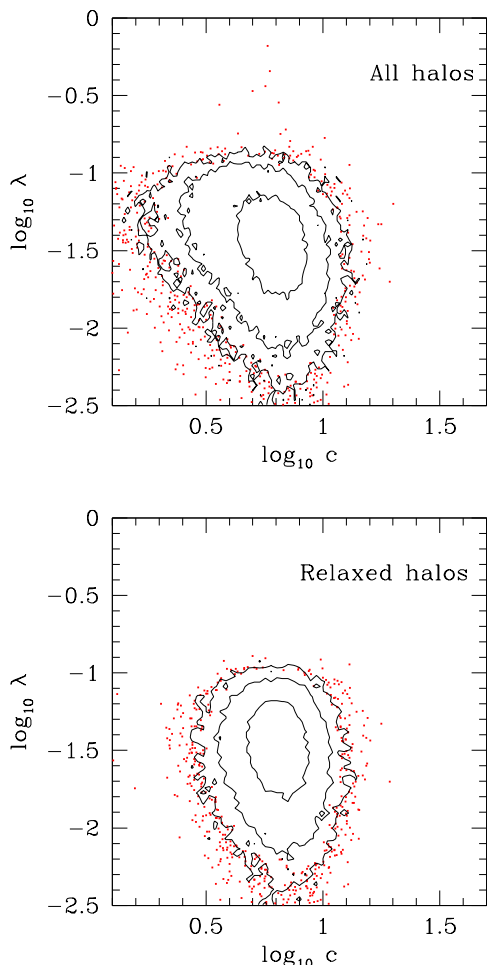


**Figure 9.** The dependence of the spin parameter on concentration for the full halo sample (top panel) and for *relaxed* haloes (bottom panel). The iso-density contours enclose 65, 95 and 99% of the distribution while the individual points show the distribution for the remaining 1% of the distribution.

ticularly important during mergers, and leads to an overall reduction of  $\lambda$  as the merger progresses (see also Gardner (2001); Vitvitska et al. (2002)).

We conclude, in agreement with M07, that the bulk of the effect reported by Bailin et al. (2005) is due to the inclusion of out-of-equilibrium haloes in their sample. A very weak correlation between  $c$  and  $\lambda$  may be visible in the tilt of the contours in the *relaxed* halo panel of Fig. 9, but it seems too weak to have strong observational implications.

### 3.3 Concentration vs formation time

The mass-concentration dependence was originally interpreted by NFW as the result of the dependence of halo formation time on mass: the halo characteristic density just reflects the mean density of the Universe at the time of collapse. Therefore, low-mass haloes are more concentrated because they collapsed earlier, when the Universe was denser.

NFW also showed that the bulk of the scatter in the concentration at given mass is due to variations in formation redshift. In this section we revisit the NFW analysis using our simulations.

The first thing to note is that there is no unique way of defining when a particular halo formed, and so different definitions have been adopted (Lacey & Cole 1993; Navarro, Frenk, & White 1997; Wechsler et al. 2002; Zhao et al. 2003a). The simplest and most widely used definition is to set the formation redshift of a halo as the time when the most massive progenitor first exceeds half of the final halo mass,  $M(z_f) = M(z=0)/2$ . We use this as our default definition, but we will also consider other variants below.

Fig. 10 shows the dependence of the formation redshift (expressed as  $1+z_f$ ) on halo mass. As expected, the median formation redshift clearly declines with increasing mass, and the solid line in the figure shows a least-squares fit to the median concentration. Dots show a random selection of haloes coloured according to their concentration. The gradual change in colour from top to bottom indicates that concentration and formation time are closely related.

We investigate this further in Fig 11, where we plot the offset in concentration from the mean mass-concentration relation (Fig. 6) versus the formation redshift offset from the mean mass-formation redshift relation (Fig. 10) for two mass bins. The strong correlation between residuals indicates that the scatter in concentration at fixed mass is mostly due to variations in formation time.

The fraction of the scatter in concentration shown in Fig. 7,  $\sigma_{\text{lgM}}$ , accounted for by  $z_f$  variations may be estimated by comparing it with the rms scatter,  $\sigma_{\text{lgzf}}$ , about the 1:1 line in Fig. 11. The fractional reduction in the variance,  $|\sigma_{\text{lgM}}^2 - \sigma_{\text{lgzf}}^2|/\sigma_{\text{lgM}}^2$  is 35% for the lowest mass range,  $10^{11.75} < M_{200}/h^{-1}M_{\odot} < 10^{12.25}$ , and 12% for the highest mass range,  $10^{14.25} < M_{200}/h^{-1}M_{\odot} < 10^{14.75}$ .

This implies that the scatter in concentration is not fully explained by differences in formation time alone, and that additional effects are at work. One possibility is that the additional scatter is an environmental effect, as recently proposed by Wechsler et al. (2006). However, these authors find that the effect is restricted to low-mass haloes, whereas our results show additional scatter for high mass haloes as well.

Another possibility is that our formation time definition should be revised. After all, the fraction of halo mass enclosed within the scale radius,  $r_s$  (which defines  $c$ ), is *much less* than one-half of the halo mass for the typical concentrations shown in Fig. 6. Or, finally, it might be that the scatter is driven by some aspect of the merger history that is not fully captured by our default definition of  $z_f$ , which depends on a single component of the halo (its most massive progenitor) rather than on the full spectrum of fragments that coalesce to form the final halo.

We explore this in Fig. 12, where we compare the NFW characteristic density,  $\delta_c$ , with four different definitions of the formation redshift. We use  $\delta_c$  in this figure because, besides being equivalent to the concentration,  $c$ , it is easier to interpret. Indeed, if the characteristic density really tracks the mean density of the universe at the time of formation, one would expect it to follow the “natural” scaling,  $\delta_c \propto (1+z_f)^3$ .

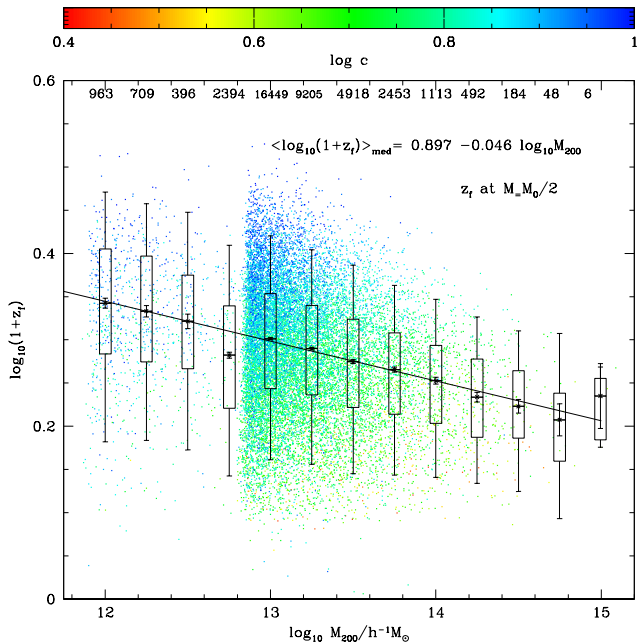


**Figure 10.** Halo formation time as a function of mass for *relaxed* haloes. Formation times are defined as the time when the most massive progenitor reaches half of the final halo mass. The numbers along the top of the main panel indicate the number of haloes in each bin. The straight line is a least square fit to the median concentration. The colour of the plotted points encodes the concentration as indicated by the colour bar. The gradual change in colour, from green in the upper region of the plot to red at the bottom, shows qualitatively that concentration depends sensitively on the formation time. See also Fig. 11.

Three of the  $z_f$  definitions explored in Fig. 12 are variations of the one adopted above, and indicate the time when the most massive progenitor first exceeds 10, 25, and 50% of the final halo mass,  $M_0 = M(z = 0)$ . These correspond to the panels labelled  $M_0/10$ ,  $M_0/4$ , and  $M_0/2$  in Fig. 12, respectively. The last definition, on the other hand, follows the prescription of NFW, and identifies the time when the *combined mass* of all  $M > M_0/10$  progenitors exceeds  $M_0/2$ .

As is clear from Fig. 12, the tightest relation around the “natural scaling” (shown as solid lines) corresponds to the NFW definition. This suggests that the full mass spectrum of clumps that assemble into the halo plays an important role in the final halo concentration and not just the most massive progenitor.

We also note that in each panel of Fig. 12 it is the first (lowest redshift) bin that has the largest scatter and that is furthest from the “natural scaling” relation. This bin corresponds to haloes that have been assembled very recently, and may contain haloes that, despite our selection criteria, are still unrelaxed and for which the structural parameters are ill defined.

### 3.4 Concentration predictions

It is clear from the above discussion that accurate predictions of the concentration require some knowledge of the halo’s assembly history. This cautions against the common

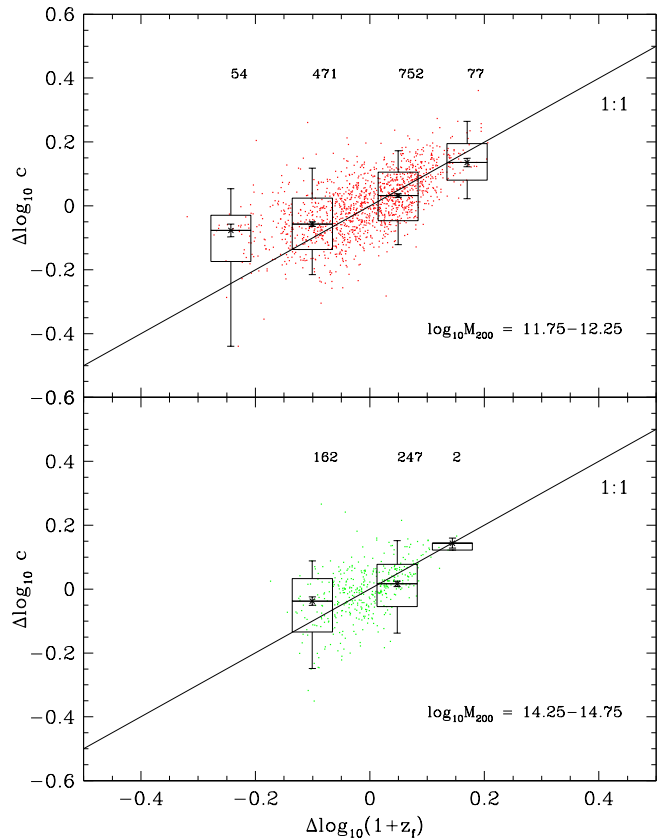


**Figure 11.** Concentration offsets from the mean mass-concentration relation (Fig. 6) versus formation-time offsets from the mean mass-formation time relation (Fig. 10) for two mass bins, as labelled in each panel. The strong correlation between residuals implies that much of the scatter in the  $M$ - $c$  relation is due to variations in the formation time of haloes of given mass. Boxes indicate the median and (25,75) percentiles, whiskers stretch to the (5,95) percentiles. The number of haloes in each  $\Delta \log_{10}(1+z_f)$  bin is given in the legend.

practise in semi-analytic models of assigning concentrations to haloes according to just their mass and to some probabilistic accounting of the dispersion shown in Fig. 7. As emphasised by Gao, Springel, & White (2005), properties such as the clustering of haloes depend on the assembly history, so a full description of the correlation between formation history and concentration may affect significantly the model predictions for the size and internal structure of a galaxy.

A couple of prescriptions designed to predict halo concentrations at  $z = 0$  from their mass accretion histories have been proposed recently (W02, Z03), and we use our simulation merger trees in order to compare them. We focus on the *relaxed* halo sample, since these have well-defined concentration parameters. We also compare these methods with the simple prescription originally proposed by NFW.

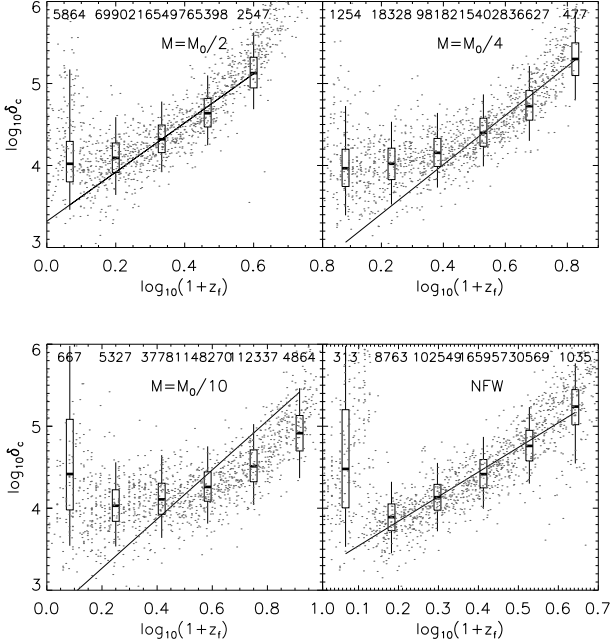


**Figure 12.** The correlation between the halo characteristic density,  $\delta_c$ , and different definitions of formation time for *relaxed* haloes. The numbers along the top of each panel indicate the number of haloes in each bin. In the first three panels the formation time is defined by reference to the most massive progenitor, and is set to be the redshift at which its mass was  $1/2$ ,  $1/4$  or  $1/10$  of the final halo mass,  $M_0$  (see labels in each panel). In the final panel (labelled NFW) the formation time is defined as the redshift when half of the final halo mass is in progenitors more massive than  $1/10$  of  $M_0$ . The “natural scaling”  $\delta_c \propto (1+z_f)^3$  is indicated by the solid line in each panel.

### 3.4.1 Wechsler et al. prescription

W02 showed that the Mass Accretion History (MAH) of a halo’s most massive progenitor, of mass  $M_0$  at redshift  $z = 0$ , may be approximated by a simple function,

$$\log_{10} M(z) = \log_{10} M_0 - \alpha z \quad (7)$$

i.e., by a straight line with slope  $-\alpha$  in the plane  $\log_{10} M(z)$  vs.  $z$  (see also van den Bosch (2002)). These authors then relate the parameter  $\alpha$  to a formation time via  $a_f = 1/(1+z_f) = \alpha/2 \ln(10)$ . Their Fig. 6 shows that this definition of formation time correlates well with the halo concentrations measured by B01 in their simulations and can be used to predict  $c$  at  $z = 0$ .

Fitting this correlation, they find

$$c_w = c_0/a_f, \quad (8)$$

with  $c_0 = 4.1$ , the typical concentration of haloes forming at the present time. The implementation of this prescription in our simulations is straightforward, and we show the predictions in Fig. 13, after recalibrating eq. 8 with  $c_0 = 2.26$  in order to take into account our different definition of virial radius.

### 3.4.2 Zhao et al. prescription

Z03 differentiate two distinct phases in the MAH; one of early, fast accretion, followed by a slow-accretion period that lasts until the present. The transition between the two phases occurs at a characteristic redshift,  $z_{\text{tp}}$ . This “turning-point” redshift may be used to estimate the concentration, assuming that the inner properties of the halo, such as the scale radius,  $r_s$ , and its enclosed mass, are set at  $z_{\text{tp}}$  and vary weakly thereafter.

This procedure is in principle straightforward to implement in our simulations but we note that there are a substantial number of haloes for which the distinction between the two accretion phases is not well-defined. In some cases, more than one phase of fast accretion seems to be present; in others, there is a single phase with no obvious turning point. This leads to ambiguities in the definition of  $z_{\text{tp}}$  and its associated concentration that are not easily resolved and that affect a significant fraction of haloes. A similar worry applies to the Wechsler et al prescription, since eq. 7 is a poor approximation to the MAH of a significant number of systems.

### 3.4.3 NFW prescription

Finally, we consider NFW’s proposal to identify the formation redshift with the epoch when 50% of the halo is contained in progenitors more massive than certain fraction,  $f$ , of the final halo mass. NFW propose  $f = 0.01$  in their original work in order to match the mass-concentration relation using the extended Press-Schechter formalism, but this fraction is too low to allow for an accurate estimate in N-body simulations. As a compromise, we adopt  $f = 0.1$  for the results shown here.

### 3.4.4 Comparison between prescriptions

Note that the three prescriptions described above are based on different features of the halo merger trees. While NFW looks at the mass spectrum of clumps containing half of the final halo mass, the other methods consider just the MAH of the most massive progenitor. The Z03 prescription depends on the slope of the scaling relation  $\log_{10} M_s$  vs.  $\log_{10} r_s$  in the slow accretion phase while the W02 recipe fits the whole MAH with a single slope.

In spite of these differences, Fig. 13 shows that all three procedures yield concentrations that correlate reasonably well with the measured values. The rms scatter between prediction and measurement is indicated in each panel. It is smallest (marginally) for the NFW prescription, but even in this case it only reduces the scatter in the mass-concentration relation (Fig. 6) from  $\sigma_{\text{IGM}} = 0.092$  to  $\sim 0.077$ . Thus it only accounts for about 30% ( $(\sigma_{\text{IGM}}^2 - \sigma_{\text{NFW}}^2)/\sigma_{\text{IGM}}^2$ ) of the variance in the mass-concentration relation.

The W02 prescription does similarly well by this measure, but the slope of the  $c_{\text{pred}} - c_{\text{measured}}$  relation is a bit too shallow. The Z03 prediction has more scatter, but this is entirely due to a tail of haloes for which it predicts very low concentrations. We conclude that all three methods predict concentrations that correlate well with the measured values, but none of them is able to fully account for the scatter in the mass-concentration relation.

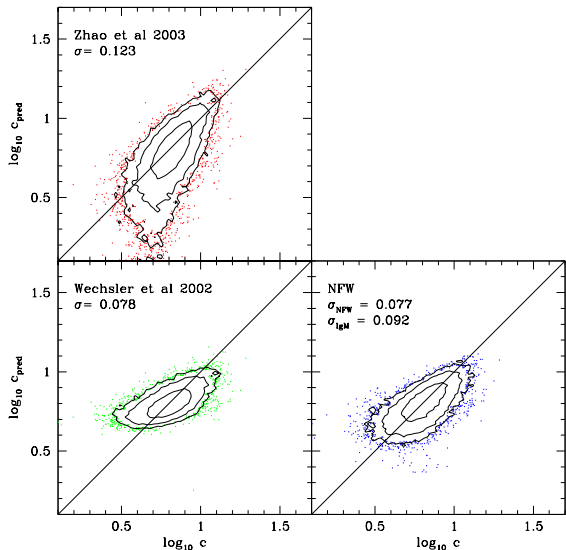


**Figure 13.** A comparison of the measured concentrations with those predicted by the Zhao et al. (2003a) (top), Wechsler et al. (2002) (bottom left) and NFW (bottom right) prescriptions. The plotted contours enclose 65%, 95% and 99% of the haloes with the remaining 1% plotted as points. The  $\sigma$ -values indicated in each panel give the rms scatter in the prediction  $((\log_{10}(c/c_{\text{pred}}))^2)^{1/2}$ , while  $\sigma_{\text{IGM}}$  is the corresponding rms scatter about the mass-concentration relation for the same set of haloes.

#### 4 SUMMARY

We use the *Millennium Simulation* to examine the structural parameters of dark matter haloes formed in the  $\Lambda$ CDM cosmogony. The large volume probed by the *MS*, together with its unprecedented numerical resolution, allow us to probe confidently the mass profiles of haloes spanning more than three decades in mass. Our main conclusions may be summarised as follows.

- As in earlier studies, we find that the mass profile of dynamically *relaxed* haloes are well approximated by the two-parameter NFW profile. We find that at least 1000 particles are needed in order to obtain unbiased estimates of the distribution of halo concentrations and illustrate a number of potential pitfalls that arise from analysing poorly-resolved haloes, or from including in the sample haloes manifestly out of equilibrium.

- We study the correlation between the NFW fit parameters, which we express in terms of the halo mass and a concentration parameter. These results extend previous studies to much larger halo masses than hitherto reported in the literature. Combining our results with those of Macciò et al. (2007), we find that a single power law reproduces the mass-concentration relation for over six decades in mass. These results are in reasonable, albeit not perfect, agreement with the predictions of the Eke, Navarro, & Steinmetz (2001) and NFW models. The model of Bullock et al. (2001) fails at large masses, and predicts concentrations at least a factor of  $\sim 2$  too low for  $M \sim 10^{15} h^{-1} M_{\odot}$  haloes.

- The dependence of concentration on mass, while well established, is weak, and of equal importance is the broad scatter in concentration at fixed mass. The distribution of

concentrations at given mass is well fitted by a lognormal function where *both* the mean and the dispersion decrease with increasing halo mass. These results allow us to estimate in detail the abundance of haloes with unusually low or unusually high concentration, providing a well-defined prediction that may be used to interpret observations of objects of unusual density, such as highly-effective cluster lenses or galaxies with haloes of anomalously low density.

- We find that, once *unrelaxed* haloes are excluded, there is no significant correlation between halo spin and concentration, contrary to the results of Bailin et al. (2005).

- We have searched for several ways to account for the large dispersion in concentrations at given mass. The scatter in concentrations seems to arise largely due to variations in the formation time. We examined various plausible definitions of the formation time, and find that concentrations are best predicted by formation times defined taking into account the collapse history of the full spectrum of progenitors rather than the evolution of the single most massive progenitor.

- We compare the schemes of Zhao et al. (2003a), Wechsler et al. (2002), and a variant of the NFW prescription, and find that, while all three show a strong correlation between the predicted and measured concentrations, considerable scatter remains. In fact, none of these models is able to account for more than 30% of the intrinsic variance in the mass-concentration relation. It appears as if a large fraction of the scatter is truly stochastic or, else, dependent on aspects of the halo merger history that are not probed by these simple schemes.

#### ACKNOWLEDGEMENTS

The simulation used in this paper was carried out as part of the programme of the Virgo Consortium on the Regatta supercomputer of the Computing Centre of the Max-Planck Society in Garching. AFN would like to thank for the hospitality of ICC during the year 2005 and the LENAC network for financial support. AFN would also like to acknowledge John Helly for his help with the merger trees. JFN acknowledges support from Canada's NSERC, as well as from the Leverhulme Trust and the Alexander von Humboldt Foundation. PB acknowledges the receipt of a PhD studentship from the UK Particle Physics and Astronomy Research Council.

#### REFERENCES

- Avila-Reese V., Firmani C., Klypin A., Kravtsov A. V., 1999, *MNRAS*, 310, 527
- J. Bailin, C. Power, B. K. Gibson and M. Steinmetz, arXiv:astro-ph/0502231.
- Bett P., Eke V., Frenk C. S., Jenkins A., Helly J., Navarro J., 2007, *MNRAS*, 376, 215
- Bower R. G., Benson A. J., Malbon R., Helly J. C., Frenk C. S., Baugh C. M., Cole S., Lacey C. G., 2006, *MNRAS*, 370, 645
- Bullock J. S., Kolatt T. S., Sigad Y., Somerville R. S., Kravtsov A. V., Klypin A. A., Primack J. R., Dekel A., 2001, *MNRAS*, 321, 559

**Table 1.** Parameters of the log-normal fits (eq. 6) to the distribution of concentrations as a function of mass for bins shown in Fig. 6. The first two columns are the halo mass,  $M_{200}$ , and the number of haloes in each mass bin. The following two columns denote the median and dispersion in the logarithm of the concentration;  $\langle \log_{10} c_{200} \rangle$ , and  $\sigma_{\log_{10} c}$  for the *relaxed* halo sample. The last three columns are the fraction of unrelaxed haloes,  $f_{\text{unrel}}$ , as well as the median and dispersion in the logarithm of the concentration for that sample.

$\log_{10} M_{200}$ [ $h^{-1} M_{\odot}$ ]	$N_{\text{haloes}}$	$\langle \log_{10} c \rangle$ [relaxed]	$\sigma_{\log_{10} c}$ [relaxed]	$f_{\text{unrel}}$	$\langle \log_{10} c \rangle$ [unrelaxed]	$\sigma_{\log_{10} c}$ [unrelaxed]
11.875 - 12.125	911	0.920	0.106	0.205	0.683	0.147
12.125 - 12.375	721	0.903	0.108	0.171	0.658	0.150
12.375 - 12.625	403	0.881	0.099	0.199	0.646	0.139
12.625 - 12.875	165	0.838	0.101	0.229	0.605	0.158
12.875 - 13.125	13589	0.810	0.100	0.263	0.603	0.136
13.125 - 13.375	9194	0.793	0.099	0.253	0.586	0.140
13.375 - 13.625	4922	0.763	0.095	0.275	0.566	0.142
13.625 - 13.875	2474	0.744	0.094	0.318	0.543	0.140
13.875 - 14.125	1118	0.716	0.088	0.361	0.531	0.131
14.125 - 14.375	495	0.689	0.095	0.383	0.510	0.121
14.375 - 14.625	191	0.670	0.094	0.370	0.490	0.133
14.625 - 14.875	49	0.635	0.091	0.484	0.519	0.121
14.875 - 15.125	8	0.664	0.061	0.578	0.493	0.094

- Cole S., Lacey C., 1996, MNRAS, 281, 716  
Colless M., et al., 2001, MNRAS, 328, 1039  
Davis M., Efstathiou G., Frenk C. S., White S. D. M., 1985, ApJ, 292, 371  
de Blok W. J. G., Bosma A., McGaugh S., 2003, MNRAS, 340, 657  
D’Onghia E., Navarro J. F., 2007, astro, arXiv:astro-ph/0703195  
Eke V. R., Cole S., Frenk C. S., 1996, MNRAS, 282, 263  
Eke V. R., Navarro J. F., Steinmetz M., 2001, ApJ, 554, 114  
Gao L., White S. D. M., Jenkins A., Stoehr F., Springel V., 2004, MNRAS, 355, 819  
Gao L., Springel V., White S. D. M., 2005, MNRAS, 363, L66  
Gardner J. P., 2001, ApJ, 557, 616  
Ghigna S., Moore B., Governato F., Lake G., Quinn T., Stadel J., 2000, ApJ, 544, 616  
Harker G., Cole S., Helly J., Frenk C., Jenkins A., 2006, MNRAS, 367, 1039  
Jing Y. P., 2000, ApJ, 535, 30  
Klypin A., Kravtsov A. V., Bullock J. S., Primack J. R., 2001, ApJ, 554, 903  
Kravtsov A. V., Klypin A. A., Khokhlov A. M., 1997, ApJS, 111, 73  
Lacey C., Cole S., 1993, MNRAS, 262, 627  
Lahav O., Lilje P. B., Primack J. R., Rees M. J., 1991, MNRAS, 251, 128  
Limousin M., et al., 2006, arXiv:astro-ph/0612165  
Macciò A. V., Dutton A. A., van den Bosch F. C., Moore B., Potter D., Stadel J., 2007, MNRAS, 378, 55  
McGaugh S. S., Barker M. K., de Blok W. J. G., 2003, ApJ, 584, 566  
Navarro J. F., Frenk C. S., White S. D. M., 1995, MNRAS, 275, 720  
Navarro J. F., Frenk C. S., White S. D. M., 1996, ApJ, 462, 563  
Navarro J. F., Frenk C. S., White S. D. M., 1997, ApJ, 490, 493  
Percival W. J., et al., 2001, MNRAS, 327, 1297  
Power C., Navarro J. F., Jenkins A., Frenk C. S., White S. D. M., Springel V., Stadel J., Quinn T., 2003, MNRAS, 338, 14  
Shaw L. D., Weller J., Ostriker J. P., Bode P., 2005, AAS, 37, 1330  
Spergel D. N., et al., 2003, ApJS, 148, 175  
Spergel D. N. et al., arXiv:astro-ph/0603449v2  
Springel V., White S. D. M., Tormen G., Kauffmann G., 2001, MNRAS, 328, 726  
Springel V., et al., 2005a, Nature, 435, 629  
Springel V., 2005b, MNRAS, 364, 1105  
Thomas P. A., Muanwong O., Pearce F. R., Couchman H. M. P., Edge A. C., Jenkins A., Onuora L., 2001, MNRAS, 324, 450  
van den Bosch, F. C. 2002, MNRAS, 331, 98  
Vitvitska M., Klypin A. A., Kravtsov A. V., Wechsler R. H., Primack J. R., Bullock J. S., 2002, ApJ, 581, 799  
Wechsler R. H., Bullock J. S., Primack J. R., Kravtsov A. V., Dekel A., 2002, ApJ, 568, 52  
Wechsler R. H., Zentner A. R., Bullock J. S., Kravtsov A. V., Allgood B., 2006, ApJ, 652, 71  
Zhao D. H., Mo H. J., Jing Y. P., Börner G., 2003a, MNRAS, 339, 12  
Zhao D. H., Jing Y. P., Mo H. J., Börner G., 2003b, ApJ, 597, L9